Fragmentation of polarized ^{23}Na on ^{208}Pb and the random-walk model

N. M. Clarke, O. Karban, C. O. Blyth, H. D. Choi, S. J. Hall, S. Roman, and G. Tungate
School of Physics & Space Research, University of Birmingham, Birmingham B15 2TT, England

A. J. Cole
Institut des Sciences Nucléaires, Institut National de Physique Nucléaire et de Physique des Particules, 53, Rue des Martyrs, Grenoble, France

N. J. Davis and A. C. Shotter
Department of Physics, University of Edinburgh, Edingburgh, EH9 3JZ, Scotland

K. A. Connell
Science and Engineering Research Council, Daresbury Laboratory, Warrington, WA4 4AD, England
(Received 20 January 1992)

Inclusive measurements are presented for the differential cross sections and tensor analyzing powers ($^{T}T_{20}$ and T_{20}) of ions produced by the fragmentation of a beam of polarized ^{23}Na incident on a ^{208}Pb target at an energy of 195.5 MeV (8.5 MeV/nucleon). The data are discussed in terms of a simple "shape-effect" model, and compared to the predictions of the nuclear random-walk model which has been extended to the calculation of aligned, deformed projectiles. This model reproduces the principal features of the differential cross sections and the trends as a function of mass loss, but gives poorer agreement for the analyzing powers.

PACS number(s): 25.70.Mn, 24.70.+s, 24.60.−k

I. INTRODUCTION

The experimental measurements of collisions between two heavy ions have revealed a variety of phenomena indicative of many-body physics at its most perplexing. At energies above 100 MeV/nucleon, a huge multifragmentation takes place, resulting in large multiplicities (up to 40) of charged ions whose masses range from light ions ($Z=1,2$) to targetlike fragments (TLFs). The number of models of these phenomena has expanded to a similar multiplicity. A review of the experimental observables and the various models has been recently given by Kampert [1]. At lower energies (10–100 MeV/nucleon) the simple abrasion-ablation models [2] developed for very high energies fail to explain the data; dynamical models [3] have been used to explain the low velocity peak in the energy spectra [4], while statistical models [5–7] including compound nucleus decay [8] predict multiple fragment emission. Recent studies of the flow energy in these intermediate energy collisions [9] have ruled out evaporative processes, and other work has studied the onset of multifragmentation using the restructured aggregation model [10] coupled to the Landau-Vlasov model [11] or by extensions to the quantum molecular dynamics model [12].

The random-walk model proposed by Cole [13] extended the ideas of Karol [14] and Harvey [15] using the number of nucleon-nucleon collisions as a measure of the reaction strength, and introducing a probability matrix for nucleon loss or gain in the collision. This has been successfully applied to a number of data sets [16,17]. In this work, we present the first study of fragmentation using a beam of polarized ^{23}Na (spin $\frac{3}{2}$) incident on a ^{208}Pb target at 195.5 MeV (8.5 MeV/nucleon), measuring inclusive differential cross sections and tensor analyzing powers for all ions with $Z=3$ to 10; by modifying the random-walk model, we predict many of the observed features of the data in terms of the shape of ^{23}Na. We use the term "fragmentation" in its loosest sense; at these low energies the collision between two heavy nuclei is essentially a cold collision, and the concepts of hot nuclear matter are inappropriate. Thus we may describe the data as "deep inelastic scattering" or "projectile breakup." We cannot *a priori* be sure of the mechanism of this process, whether it takes place by evaporation from the compound nucleus, or by direct or sequential breakup of the projectile. However, our data have many characteristics of fragmentation studies made at much higher energies and we have chosen to analyze our data using the random-walk model described in Sec. III.

The random-walk model has the merit that the differential cross sections for a wide range of ejectiles can be derived by fairly simple numerical techniques from parameters directly related to the densities of the colliding nuclei. Tensor analyzing powers can then be obtained from the differences in cross sections between the cases with polarized (shape-aligned) and unpolarized (or nonaligned) projectiles [18]. This direct relationship with the nuclear shape is not easily realized in models of fragmentation, but is essential, since the ^{23}Na nucleus has a prolate deformed shape with a measured spectroscopic quadrupole moment of 10.06 ± 0.2 e fm^2 [19]. Assuming a rotational model for the $K=\frac{3}{2}$ band of a spin $\frac{3}{2}$ nucleus, this yields an intrinsic charge quadrupole moment of 50.3

e fm^2, and a charge deformation length of 1.5 fm. Using this value, Choi *et al.* [20] were able to show that the tensor analyzing powers for the elastic scattering of polarized ^{23}Na from ^{208}Pb were produced by the deformed shape of the ^{23}Na nucleus—the so-called "shape-effect" relationship [21].

Figure 1(a) illustrates the collision, and shows how the effective projectile density for a prolate nucleus becomes smaller when the beam is transverse polarized (aligned) to place the spin symmetry axis perpendicular to the scattering plane. When ^{23}Na is aligned, the reaction cross section is *smaller,* but the elastic cross section is *larger* [21] than when there is no alignment, leading to the positive transverse analyzing powers ($^{T}T_{20}$) for the elastic scattering observed by Choi *et al.* [20].

Figure 1(b) illustrates the case of a tensor polarized beam with the spin axis aligned along the direction of the beam (helicity frame). At large impact parameters, there is less overlap of the projectile density with the target when it is aligned than when it is not aligned, but as the impact parameter decreases, the situation reverses so that we expect to see a change in the sign of the elastic analyzing powers (T_{20}), and this is confirmed by various measurements [21].

The corollary of the shape-effect model for elastic scattering would suggest that the nonelastic processes should yield analyzing powers with the opposite sign to those for the elastic scattering. Mobius *et al.* [22] saw such an effect in the values of T_{20} measured by the γ-ray yield from evaporation residues for ^{7}Li + ^{51}V which were in complete agreement with the values of T_{20} obtained for the total reaction cross section obtained from the elastic scattering data. In a study of the fusion-fission reaction of ^{23}Na + ^{138}Ba, Hall *et al.* [23] found the elastic scattering data could not be used to successfully reproduce the fission analyzing powers. The authors suggested that this resulted from an angular momentum limit to the fusion cross section rather than a geometrical limit which would lead to shape effects. A similar effect was described by Blatt *et al.* [24] who studied the high energy fusion of ^{23}Na with ^{23}Na. Our study of the fragmentation in the ^{23}Na + ^{208}Pb system aimed to measure the analyzing powers for those nonelastic processes (except fusion) which make a large contribution to the reaction cross section, and where the simple shape-effect model suggests that we should observe large analyzing powers. It is clear that the use of a polarized beam and the measurement of analyzing powers may give us information about the interaction of the projectile shape with the target which is difficult to extract from other observables.

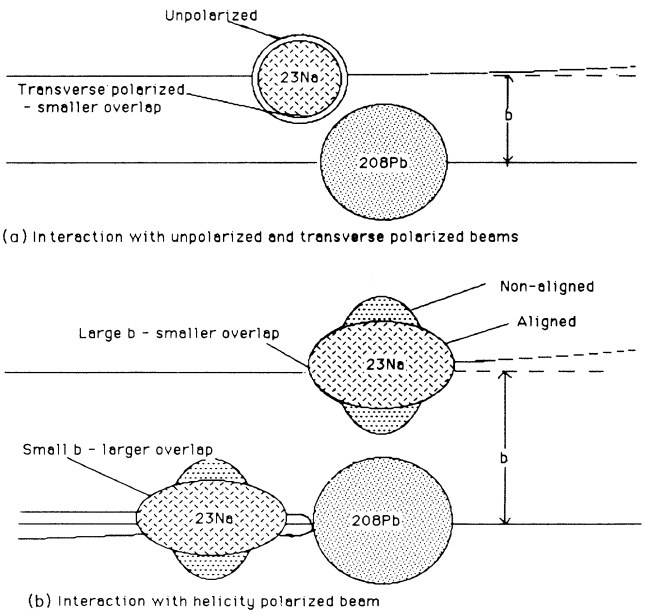

FIG. 1. Schematic diagram of the interaction of polarized ^{23}Na with ^{208}Pb. (a) Interaction with unpolarized and transverse polarized beams. (b) Interaction with a beam polarized in the helicity frame.

II. EXPERIMENT AND DATA

The operation of the polarized heavy ion source at the Nuclear Structure Facility (NSF), Daresbury Laboratory has been described by Karban *et al.* [25], and the experimental details were identical to those described by Choi *et al.* [20]. From the 2D spectra of ΔE vs E, the energy spectra for particles with different ionic charge Z could be constructed, but the resolution was insufficient [26] to separate individual isotopes corresponding to a given charge number Z. Figure 2 shows the energy spectra at 45° laboratory angle. For Na ions, the strong quasielastic peak is seen, but for Ne and F ions the energy distributions are skew with a low energy tail, then become roughly symmetric for lighter ions. For $Z \leq 5$ the lower energy part of the spectra was cut off by the ΔE detector thickness. This results in an asymmetric energy spectrum and means that the measured cross sections for these ions may be too small.

The centroid energies of the spectra at both 45° and 32° (laboratory) shown in Fig. 3 give a similar slope at both angles, with a slight curve for the lower Z ions. The dashed line is a prediction of the energies at 45°, assuming two body kinematics with the mass loss M transferred to the target, and a Q value in the reaction of

$$Q_M = -ME_L A_T / A_P (A_T + M) , \quad (1)$$

where E_L is equal to the incident energy and A_P and A_T are the mass numbers of the projectile and target. This is the Q value which would result if the fragment traveled on with the beam velocity, corresponding to a spectator model of projectile breakup [27]. The solid line in Fig. 3 shows the energies which result from the extended Brink selection rules [28], taking into account the differences in the Coulomb barriers which result from the transfer of charge during grazing collisions. As shown by Siemens and Jensen [29], this results in a Q value given by

$$Q = -M[(A_T + A_P)/A_P A_T][E_L - 1.44 Z_P Z_T / R_C] - \Delta Z[Z_T - Z_P + \Delta Z] 1.44 / R_{GR} . \quad (2)$$

The first term represents the kinetic energy of relative

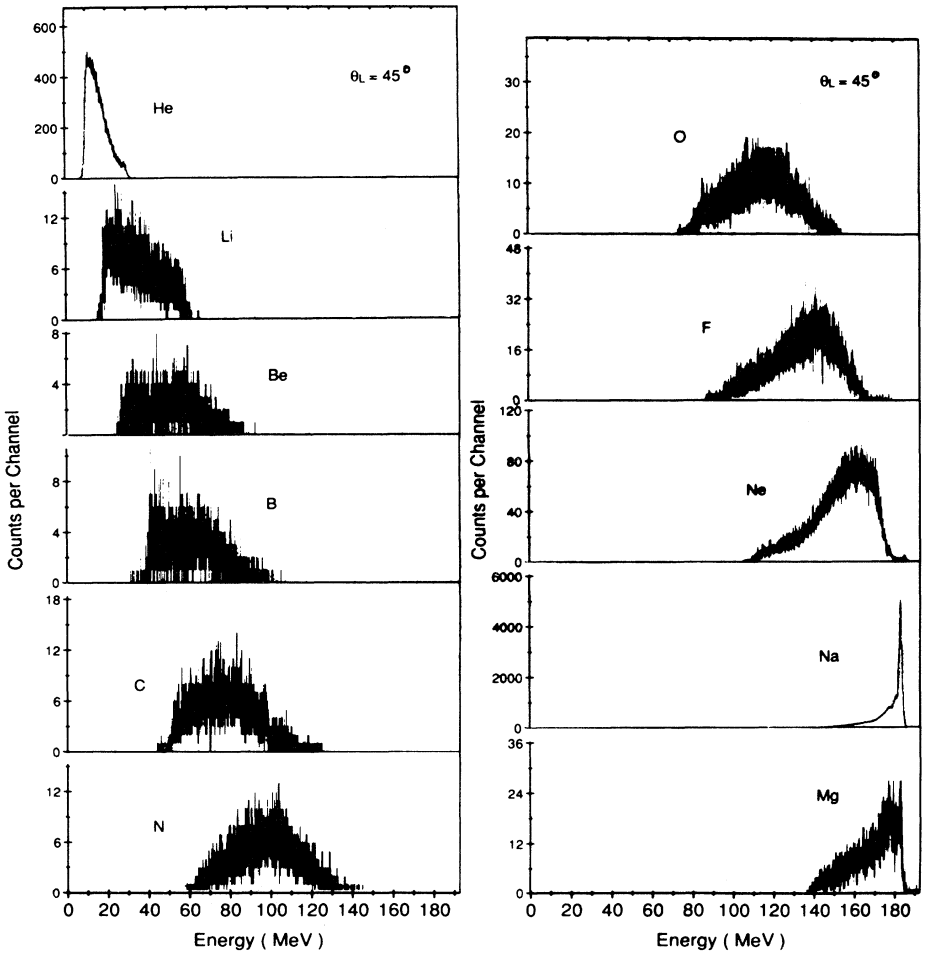

FIG. 2. Inclusive energy spectra for the fragmentation of polarized ^{23}Na on ^{208}Pb at 195.5 MeV (8.5 MeV/nucleon) at $\theta_L = 45°$.

motion which is converted to internal energy of the projectile or target, while the second term results from the difference in Coulomb barriers of the incoming and outgoing channels. Here we have assumed that the mass *loss* M is twice the charge *loss* ΔZ, and we have set $R_C = R_{GR} = 1.4[A_P^{\frac{1}{3}} + A_T^{\frac{1}{3}}]$ fm. Equation (2) assumes that the mass loss M is small compared with A_P or A_T. Harvey and Murphy [30] have described a geometrical model for the overlapping nuclei which does not require M to be small; however, Eq. (2) predicts the slope of the energy centroids quite well, but overpredicts the energies by about 8 MeV. This additional loss of energy is ascribed to exchange processes and excitation of collective states [29].

Energy integrated differential cross sections $\sigma(\theta)$ were obtained by integrating the complete energy spectra for each angle setting. For the beam polarized in the transverse frame (with the spin axis of the ^{23}Na perpendicular to the scattering plane) the differential cross sections are given by [18]

$$\sigma_{\text{pol}}(\theta) = \sigma_0 \theta[1 + \tau_{20}{}^T T_{20}(\theta) + \tau_{10}{}^T T_{10} \cos\phi + \text{3rd order}] , \quad (3)$$

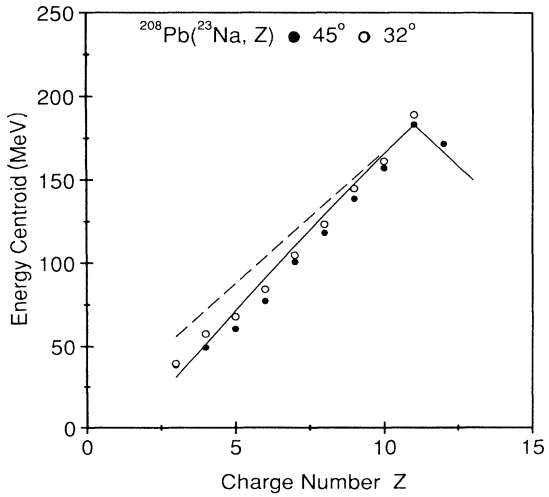

FIG. 3. Energy centroids of the inclusive spectra at 45° and 32° (laboratory). The solid line is a fit to the 45° values using the extended Brink model, while the dashed line represents the Q value which would result if the fragments traveled on with the projectile velocity.

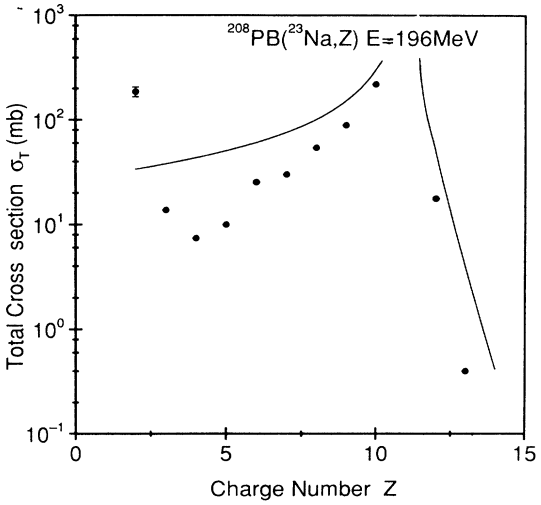

FIG. 4. Total cross section for the fragmentation of ^{23}Na vs the fragment charge, Z; the solid line is a fit from the random-walk model.

where $\sigma_0(\theta)$, $\sigma_{\rm pol}(\theta)$ correspond to the differential cross sections for unpolarized and polarized beams, respectively, and τ_{20}, τ_{10} are the tensor and vector polarizations of the beam, and θ,ϕ are the in-plane and azimuthal scattering angles. By adding data measured simultaneously on both sides of the beam axis, the vector components cancel and errors due to misalignment are negligible. The analyzing powers are obtained from

$$^{T}T_{20}(\theta)\tau_{20}=[\sigma_{\rm pol}(\theta)-\sigma_0(\theta)]/\sigma_0(\theta)\ . \quad (4)$$

Similar expressions are used to calculate the analyzing powers $T_{20}(\theta)$ for those measurements made with the beam polarized in the scattering plane.

Data were obtained for the differential cross sections over an angular range covering 18° to 60° (laboratory) inclusive, but the analyzing powers were measured over a more limited range. The angular smearing of the data is about $\pm 1.3°$ (laboratory).

Estimates of the total cross sections (lower limits) were obtained by integrating the differential cross sections over the range 18° to 60° laboratory. The total cross sections shown in Fig. 4 reveal a steady fall in value with increasing loss or gain of charge or mass from the projectile, and were less than 10 mb for B, Be, and Al. Analyzing powers for these ions therefore had very large statistical errors. Total cross sections for Li were larger than for Be, while those for He, obtained from the truncated spectra, were more than ten times larger than for Li at approximately 186 mb. The large flux of He ions results not only from the direct breakup of ^{23}Na but also the breakup of ^{8}Be ions and from evaporative processes. The ^{8}Be ions therefore do not appear in the Be spectra and thus lower the apparent cross section, but the arrival of two ^{4}He ions simultaneously in the detectors produces ΔE

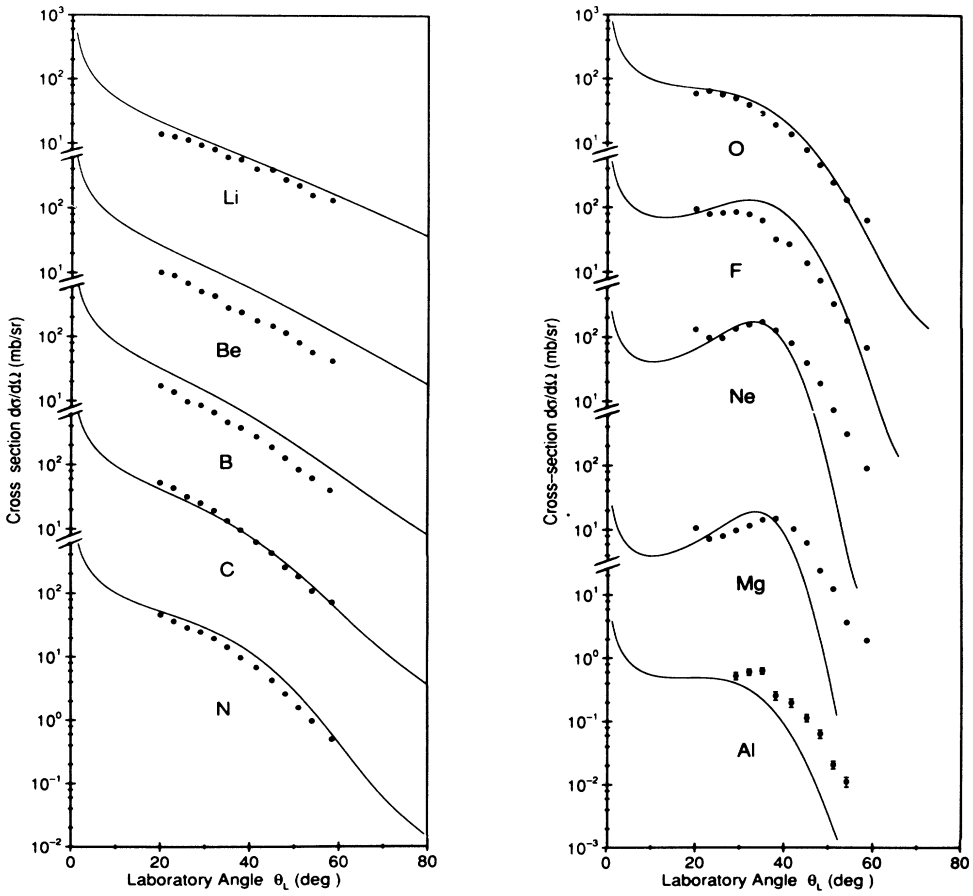

FIG. 5. Differential cross sections for the fragmentation of ^{23}Na; the solid lines are predictions from the random-walk model.

and E signals which are indistinguishable from those for ^{7}Li, and so enhance the cross section for Li ions.

The differential cross sections shown in Fig. 5 illustrate the smooth transition of shape with increasing charge loss ΔZ, or mass loss M. For small values of ΔZ, the bell-shaped distributions peak near the Coulomb rainbow angle near 40° (laboratory), but this feature gradually disappears for larger ΔZ, and a smooth exponential decline with increasing angle is seen.

A similar evolution is also seen in the transverse tensor analyzing powers (Fig. 6); for Ne these are almost zero, but negative values are seen for the F ions with suggestions of an oscillation between 50° and 60° (laboratory). The negative values are maintained or appear to increase with increasing ΔZ, with the largest values for N ions; the analyzing powers then appear to decrease for lighter ions, and are distributed about zero for Li ions. For the Be and B ions, poor statistics hampered the extraction of meaningful values of $^{T}T_{20}$.

The T_{20} data (Fig. 7) show similar characteristics to the $^{T}T_{20}$ data; small analyzing powers for Ne ions, with more negative values for N ions, tending towards small values for Li ions. The data show clear evidence of a negative to positive transition near an angle of 50° (laboratory) or 54° (c.m.). This transition occurs at a smaller angle than for the elastic scattering which is seen to occur at 70° (c.m.) in the data of Karban *et al.* [26] in agreement with predictions of the shape-effects relationships [21,31].

The $^{T}T_{20}$ analyzing powers are the easiest to interpret in terms of the simple shape-effect model discussed in Sec. I. Because the overlap of the projectile and target is smaller when the beam is aligned, we expect analyzing powers for the fragmentation of opposite sign to those of the elastic scattering. Our simple shape-effect model would suggest that the overlap of projectile with target is essentially very peripheral for Ne ions, but increases with the mass lost from the projectile; for N ions, the overlap is most sensitive to the deformed shape of ^{23}Na, but for Li ions the overlap is so large that there is little effect from the deformation. This suggests that larger mass loss from the projectile corresponds to smaller impact parameters.

In fact, one should not compare the analyzing powers, but the product of the analyzing power and the cross section, which represents the change in cross section between two polarization states of the beam. Figure 8 shows the product of the experimental analyzing powers and cross sections summed over all ions with $Z=3$ to 10, and compares it with the same product for the elastic scattering measured in this experiment. In this instance the total fragment cross section was normalized to the estimated total reaction cross section. Figure 8 shows that the spin dependence of the flux loss from the elastic channel is similar to that of the flux gain in the reaction chan-

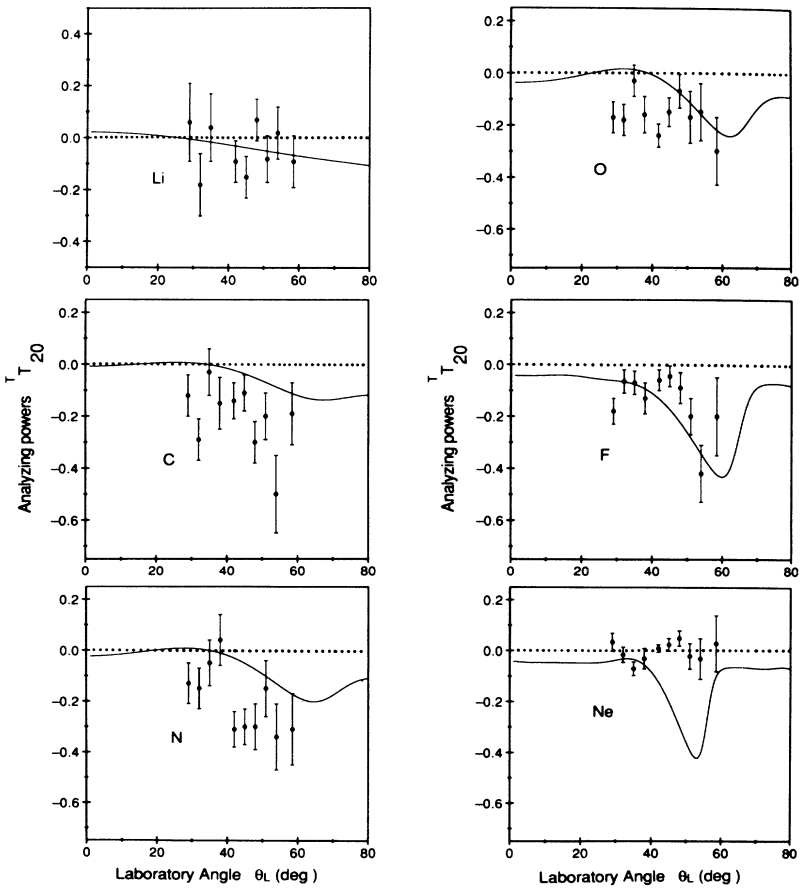

FIG. 6. Transverse ($^{T}T_{20}$) analyzing powers for the fragmentation of ^{23}Na; the solid lines are predictions from the random-walk model.

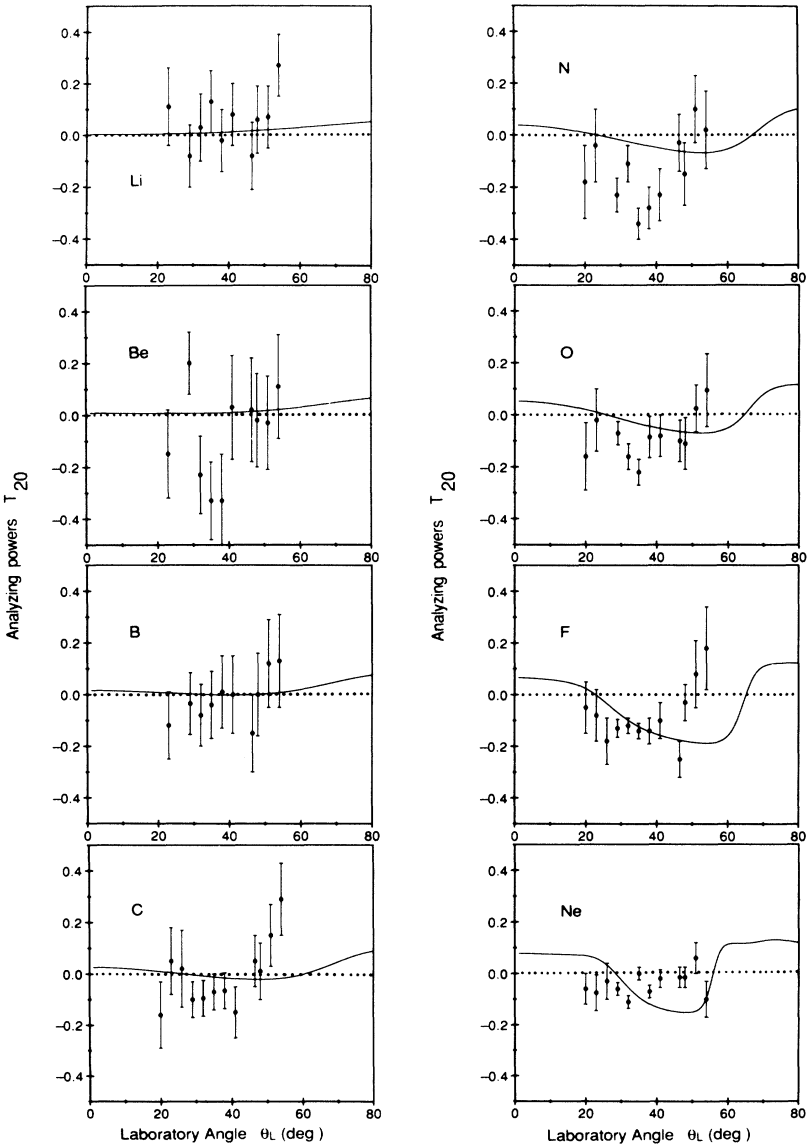

FIG. 7. Helicity (T_{20}) analyzing powers for the fragmentation of ^{23}Na; the solid lines are predictions from the random-walk model.

nels. The product of the analyzing power and cross section for the fragments is generally negative, opposite to the positive values for the elastic scattering. This supports the assumption of average fragment trajectories almost independent of fragment mass, and also average fragment analyzing powers typical of the analyzing power for the total reaction cross section.

Figure 9 shows the product of cross section and T_{20} summed over all fragments (with $Z=3$ to 10) compared with the same product for the elastic scattering. Again, the fragment values are normalized to the estimated total reaction cross section, and are seen to be of opposite sign to those for the elastic scattering, except for the datum at 32° (laboratory).

III. THE RANDOM-WALK MODEL

In this model the effects of a nucleus-nucleus collision at a given impact parameter are considered to be the result of a random walk in the projectile mass. As the projectile and target densities begin to overlap along a certain trajectory, nucleon-nucleon (N-N) collisions take place which result in a reduction of the projectile energy and either scattering, loss, or gain of nucleons within the projectile. At each step in the collision, therefore, the mass of the projectile may change in a random fashion, with the number of steps being obtained from a Poisson distribution around the average number of N-N collisions calculated in the optical limit of the Glauber theory [14]. Clearly, the average instantaneous collision rate must be proportional to the overlap of the nuclear densities, and the model makes the simplifying assumptions that the overlapping densities are those of the projectile and target, irrespective of whether any mass is lost or gained. The calculation of the observables from the collision number relies on two essential elements: the approximation of the average number of N-N collisions as a function of impact parameter, b, by a Gaussian function as

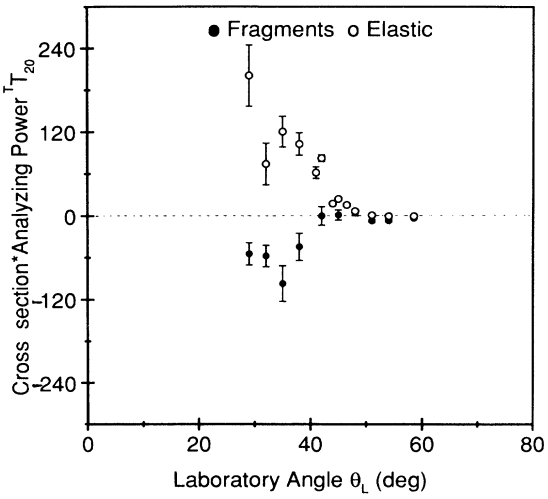

FIG. 8. Comparison of the product of cross section and transverse ($^{T}T_{20}$) analyzing powers for all ions of $Z=3$ to 10 with those for the elastic scattering at 196 MeV. The total fragment cross section was normalized to the estimated total reaction cross section.

first suggested by Karol [14], and the assumption of constant competing probabilities for nucleon loss or gain which modifies the Poissonian probability density for N-N collisions as suggested by Cole [13,16]. The details of the model are set out in Sec. III A. In all of the previous work using this model, the projectile and target were assumed to be spherical, and the projectile trajectories were assumed to be parallel to the beam direction since at high energies the effect of the Coulomb potential is reduced. This work considers the modifications to the Karol approximation for deformed, aligned projectiles in

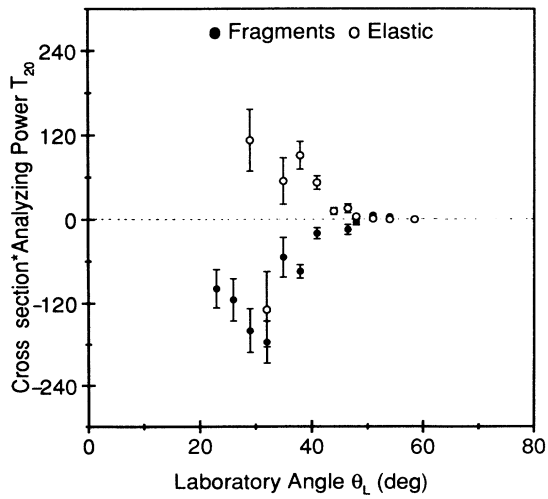

FIG. 9. Comparison of the product of cross section and helicity (T_{20}) analyzing powers for all ions of $Z=3$ to 10 with those for the elastic scattering at 196 MeV. The total fragment cross section was normalized to the estimated total reaction cross section.

Sec. III B, and the effect of Coulomb corrections to the calculations of the N-N collisions in Sec. III C.

A. N-N collisions, probabilities, and observables in the random-walk model

The average number of N-N collisions T as a function of impact parameter b is

$$\langle n \rangle = T(b) = \sigma_{NN} \int_{z=0}^{\infty} dz \int_{\mathbf{r}_P} [\rho_P(\mathbf{r}_P)\rho_T(\mathbf{r}-\mathbf{r}_P)d\mathbf{r}_P] \ , \tag{5}$$

where σ_{NN} is the isospin averaged value of the free cross section, taken as 47 fm^2 here [16]. The relative motion between projectile and target is assumed to lie in a straight line along the z axis (beam direction), and $z^2+b^2=r^2$. The second integral is the convolution of the projectile and target densities and can be readily evaluated using a double folding model code such as DFPOT [32] with a delta function for the interaction. This convolution integral then forms part of the input for the code KAROL, which performs the integration in Eq. (4). The integral in the z direction is evaluated as a function of b using Simpson's rule integration staring at $z=0$ and terminating when $(b^2+z^2)^{1/2}$ exceeded $r_{\max}$. A check of the integral over the convolution is made to ensure that it is equal to the product $A_P A_T$.

The calculation of experimental observables is simplified by Karol's approximation which employs a Gaussian form for the convolution integral; this results in an approximation for Eq. (5)

$$T_G(b) = K\sigma_{NN} \exp[-b^2/(2\sigma^2)] \tag{6}$$

valid at large impact parameters, where K and σ characterize the projectile-target combination. For each value of b, the logarithmic derivative dT/T is calculated; since for a Gaussian

$$dT/T = -b\, db/\sigma^2 \tag{7}$$

the values of σ may be found. Equating $T(b)$ to $T_G(b)$ of Eq. (6) enables K to be obtained. At the same time, the partial contributions to the reaction cross section are obtained from

$$d\sigma_R = 2\pi b\, db(1-P_n) \quad \text{with } n=0 \tag{8}$$

where

$$P_n = T^n \exp(-T)/n! \tag{9}$$

is the probability for n collisions. The total value of σ_R, obtained by summation, can be compared with the value obtained from the Gaussian geometry [14]

$$\sigma_{RG} = 2\pi\sigma^2[\ln(K\sigma_{NN})+\gamma] \tag{10}$$

where $\gamma=0.577$ is Euler's constant. The value of σ_{RG} approaches that for σ_R near $b=12$ fm in our calculations, where σ has a shallow minimum. K reaches its maximum value corresponding to the impact parameter where $T(b)\sim 1.0$.

A better approximation to Eq. (7) is

$$dT/T=-(b\,db/\sigma^2)\exp(-kT/\sigma_{NN}) , \quad (11)$$

which suppresses the Gaussian approximation for small impact parameters, and leads to the relation between T_G and b of

$$b^2/(2\sigma^2)=\mathrm{Ei}[kT(0)/\sigma_{NN}]-\mathrm{Ei}[kT(b)/\sigma_{NN}] , \quad (12)$$

where Ei is the exponential integral function. For small T at large b, the exponential integral is given by $\mathrm{Ei}(x)\sim\ln(x)+\gamma$ which is the Gaussian form. Thus by using the values of σ and K, and matching at a smaller radius, the value of k can be obtained. The pure Gaussian approximation can be restored by setting k to a small number, e.g., 1.0×10^{-8}.

Once the values of K and σ have been obtained with the code KAROL, the experimental observables can be calculated using the code FRAG.

The laboratory angle corresponding to each impact parameter is established using

$$\theta_N=-bTJ_N/(2\sigma^2E_{\mathrm{lab}}\sigma_{NN}) , \quad (13)$$

where θ_N is the angular deflection from the nuclear force to first order and J_N is the volume integral of the nucleon-nucleon potential which is assumed zero range; a value of 400 MeV fm^{-3} was used in this work. E_{lab} is the laboratory energy of the incident projectile. The Coulomb deflection is calculated from

$$\theta_C=2\tan^{-1}[Z_PZ_Te^2/(2bE_{\mathrm{lab}})] \quad (14)$$

and the total laboratory angle is $\theta_{\mathrm{lab}}=\theta_N+\theta_C$. For small values of $T(b)$ the deflection angle is positive; as T gets larger (and b gets smaller), θ_C gets more positive, and θ_N gets more negative leading to a maximum angle of deflection—the Coulomb rainbow angle θ_{CR}. At large T (small b), θ_N dominates to produce negative deflections. Both branches of the deflection function must be summed to calculate the cross sections.

The values of $dT/d\theta_{\mathrm{lab}}$ are used to calculate the differential reaction cross section

$$d\sigma/d\theta_{\mathrm{lab}}=2\pi\sigma^2(dT/d\theta_{\mathrm{lab}})\exp(kT/\sigma_{NN}) . \quad (15)$$

The code FRAG calculates the deflection angles and total reaction cross sections for values of b corresponding to $T=0.02$ collisions to a $T_{\max}$ of about 150; this produces values for the angles which are closely clustered around θ_{CR}. In order to produce angular distributions at regular intervals, the cross sections must be interpolated.

The Poisson distribution for the probability density P_n [Eq. (9)] is modified in the random-walk model by assigning the probabilities P_{-1}, P_{+1}, and P_0, respectively, for single nucleon loss, gain, or inelastic scattering. The probability for a given mass loss M at a given impact parameter b [or collision $T(b)$] is [13]

$$\begin{aligned}P_M(T(b))&=\sum_{nijk}P_n n!\frac{P_{-1}^iP_{+1}^jP_0^k}{i!j!k!}\delta_{i+j+k,n}\delta_{M,i-j}\\&=\left[\frac{P_{-1}}{P_{+1}}\right]^{M/2}I_M[2T(P_{-1}P_{+1})^{1/2}]\\&\quad\times\exp[-T(P_{-1}+P_{+1})]\end{aligned} \quad (16)$$

by using Eq. (9) with $n=i+j+k$ and $M=i-j$; I_M is a modified Bessel function of order M. This may be extended to include the mass loss due to probability of emission of alpha particles [16] (denoted by P_{-4}) by

$$\begin{aligned}P_M(T(b))&=\left[\frac{P_{-1}}{P_{+1}}\right]^{M/2}\\&\quad\times\sum_{L=0}^{\infty}\left[T\frac{P_{+1}^2P_{-4}}{P_{-1}^2}\right]^L\frac{1}{L!}\\&\quad\times I_{M-4L}[2T(P_{-1}P_{+1})^{1/2}]\\&\quad\times\exp[-T(P_{-1}+P_{+1}+P_{-4})]\end{aligned} \quad (17)$$

where L is the number of α particles.[1] The differential cross section for a mass loss M

$$d\sigma_M/d\theta=(d\sigma/d\theta_{\mathrm{lab}})P_M(T(b)) \quad (18)$$

is calculated and interpolated at 1° intervals, and then folded with a Gaussian distribution to take into account the effects of recoil due to the missing mass. This Gaussian distribution has a width given by

$$\sigma_\theta^2=\sigma_G^2/p_F^2 \quad (19)$$

where p_F is the fragment momentum, and σ_G is given in terms of the Goldhaber width parameter [5] σ_0, which arises from the Fermi momentum and is normally taken as 100 MeV/c; in this work it was increased to 150 MeV/c in order to fit the data:

$$\begin{aligned}\sigma_G^2&=\sigma_0^2A_F(A_p-A_F)/(A_p-1)\ \text{for mass loss} ,\\\sigma_G^2&=\sigma_0^2A_F(A_T+A_F)/(A_T-1)\ \text{for mass gain} ,\end{aligned} \quad (20)$$

and the fragment momentum for projectile momentum p_P is

$$\begin{aligned}p_F^2&=p_P^2(A_p-A_F)^2/A_p^2\ \text{for mass loss} ,\\p_F^2&=p_P^2\ \text{for mass gain} .\end{aligned} \quad (21)$$

The effective width, σ_θ, varies from about 4.3° for a mass loss of 2 to 21° for a mass loss of 16 in the calculations presented here. The interpolated and folded values of the cross sections $d\sigma_M/d\theta$ are then used to calculate the differential cross section

$$d\sigma_M/d\Omega=(d\sigma_M/d\theta)/(2\pi\sin\theta) . \quad (22)$$

If the emission of α particles is excluded, the total cross section for mass loss M is

$$d\sigma/dM=2\pi\sigma^2/M$$

and for a mass gain of M is

$$d\sigma/dM=(2\pi\sigma^2/M)[P_{+1}/P_{-1}]^M . \quad (23)$$

---

[1]Note that Eq. (17) appears as Eq. (15) in Ref. [16], where it is wrongly printed.

In many inclusive experiments, only charge distributions are measured, so that the differential and total cross sections for a given charge Z are a summation over all possible mass losses M with a weighting which depends upon the yield of the individual masses for a given fixed charge:

$$[d\sigma_Z/d\Omega]_{\text{expt}}=\sum_M d\sigma_{Z,M}/d\Omega \ . \tag{24}$$

However, we must also recognize that the random-walk predictions of $d\sigma_M/d\Omega$ for a given mass loss M include *all* possible charges which result in the *same* mass loss, since the model does not distinguish between protons and neutrons. Since $d\sigma_M/d\Omega$ is *independent* of Z, then for some interval δZ

$$d\sigma_{Z,M}/d\Omega=(d\sigma_M/d\Omega)/\delta Z \ . \tag{25}$$

If we now assume a mass interval δM corresponding to δZ, we may replace the summation in Eq. (24) by the *average* value of $d\sigma_{Z,M}/d\Omega$ multiplied by the width of the interval δM. Hence

$$d\sigma_Z/d\Omega=(d\sigma_{Z,M}/d\Omega)\delta M=(d\sigma_M/d\Omega)\delta M/\delta Z \ . \tag{26}$$

With the assumption that $\delta M=2\delta Z$,

$$d\sigma_Z/d\Omega=2(d\sigma_M/d\Omega) \ . \tag{27}$$

The normalization factor of 2 also applies to the total cross sections in Eq. (23).

B. The nuclear densities for deformed and aligned projectiles

In order to modify Eq. (5) for deformed and aligned projectiles, we have to include these features in the calculation of $T(b)$. The densities used were those of Choi [20].

For ^{208}Pb ($A_T=208$)

$$\rho_T(r_T)=\rho_{T0}/\{1+\exp[(r_T-R_T)/a_T]\} \ , \tag{28}$$

where $R_T=6.712$ fm, $a_T=0.481$ fm, $\rho_{T0}=0.1563$ fm^{-3}, and $\langle r_T^2\rangle^{1/2}=5.498$ fm.

For ^{23}Na

$$\rho_P(r_P)=\rho_0(r_P)+Q_{Sm}\rho_2(r_P)Y_{20}(\mathbf{r}_p\cdot\mathbf{p}) \ , \tag{29}$$

where

$$\rho_0(r_P)=(A_P/Z_P)2/(\pi^{3/2}a_0^3) \times[1+2(r_P/a_0)^2+(2/5)(r_P/a_0)^4]\exp(-r_P^2/a_0^2) \ ,$$

$$\rho_2(r_P)=(16\pi/5)^{1/2}2/(\pi^{3/2}a_0^5) \times[-(1/171)(r_P/a_0)^2+(232/5985)(r_P/a_0)^4 +(2/855)(r_P/a_0)^6]\exp(-r_P^2/a_0) \ ,$$

with $a_0=1.8$ fm, $Z_P=11$, $A_P=23$, $Q_{Sm}=21.03$ fm^2. The spin vector $\mathbf{p}$ lies along the symmetry axis.

These densities were folded with a delta function to yield the convolution integral up to a maximum radius $r_{\max}=20$ fm using the code DFPOT. Three calculations were performed; one used only the spherical component $\rho_P(r)=\rho_0(r)$ of the ^{23}Na density in Eq. (5), corresponding to an unpolarized beam. The second calculation assumed a density distribution corresponding to a transverse polarized beam, and used $\rho_P(r)=\rho_0(r)-0.5Q_{Sm}(5/4\pi)^{1/2}\rho_2(r)$ in Eq. (5). Figure 1(a) illustrates this process.

The case of a tensor polarized beam with the spin axis aligned along the direction of the beam (helicity frame) is illustrated in Fig. 1(b). At large impact parameters, the effective projectile density corresponds to that for the transverse polarized beam because the angle between $\mathbf{r}_p$ and $\mathbf{p}$ in Eq. (29) is 90°. As the impact parameter decreases, the effective projectile density in the collisions becomes that along the spin axis, i.e., $\rho_P(r)=\rho_0(r)+Q_{Sm}(5/4\pi)^{1/2}\rho_2(r)$ since now the angle γ between $\mathbf{r}_p$ and $\mathbf{p}$ approaches 0° and there is now a larger overlap of the deformed ^{23}Na nucleus with the target; it is clear that there must be a smooth transition between these two situations. Mobius [33] gives a prescription for the angle between the vectors for the case of pure Coulomb scattering. However, at this energy the effects of the nuclear potential can be seen clearly in the deflection function, and we have adopted a phenomenological approach, parametrizing the angle γ by

$$\gamma=\pi/2-(\pi/2)/\{1+\exp[(b-b_0)/a_{PT}]\} \ , \tag{30}$$

where b_0 represents the impact parameter where $\gamma=45°$ and a_{PT} represents the diffuseness over which the transition takes place. This parametrization is not unreasonable since Karol [14] shows that the overlap [Eq. (5)] assumes a Gaussian form in the nuclear surface. Assuming a simple model for the collision of two hard spheres then

$$\gamma=\begin{cases}\sin^{-1}[b/(R_p+R_T)] & \text{for } b<(R_p+R_T) \ , \\ 90° & \text{for } b>(R_p+R_T) \ ,\end{cases} \tag{31}$$

and $\gamma=45°$ when $b=b_{0HS}=0.707(R_P+R_T)$. For a prolate projectile aligned along the beam axis, it is easy to see that for a given b the neighboring nuclei are separated by a greater distance, so that γ is smaller, and the transition through $\gamma=45°$ is likely to take place at a larger impact parameter. This simple picture indicates that the value of b_0 in Eq. (30) is likely to be larger than b_{0HS} and nearer the sum of the two radii R_P+R_T.

The values of K and σ in Eq. (5) were calculated by the KAROL code for the unpolarized densities (K_U and σ_U), for the transverse polarized (minor axis) densities (K_T and σ_T) and for the helicity polarized (major axis) densities (K_H and σ_H). Following Eqs. (28) and (29), the values of K and σ can be parametrized as

$$K=K_U+\Delta K 0.5(3\cos^2\gamma-1)$$

and

$$\sigma=\sigma_U+\Delta\sigma 0.5(3\cos^2\gamma-1)$$

with

$$\Delta K=(K_H-K_U) \ \text{ and } \ \Delta\sigma=(\sigma_H-\sigma_U) \tag{32}$$

for the calculation of cross sections with the tensor (helicity) polarized beam. For the calculation of cross sections with the transverse polarized beam, the values of ΔK and $\Delta\sigma$ can be set to zero, to remove any dependence on the angle γ and the values of K and σ can be set to the values of K_T and σ_T given by the KAROL calculations.

The values K_U, ΔK, σ_U, $\Delta\sigma$, b_0, and a_{PT} form the input to the code FRAG. The relationship between T and b is calculated using Eq. (12) with the values of K_U and σ_U; the value of γ in Eq. (30) is calculated and the corrected values of K and σ obtained from Eq. (32); these are then resubstituted in Eq. (12) to get corrected values of b.

Once the three sets of different cross sections have been obtained, the tensor analyzing powers can be obtained using Eq. (4).

C. Coulomb corrections to the Gaussian approximation

At low incident energies, the straight line approximation for the trajectories in the calculations of the collision number $T(b)$ is poor because the Coulomb repulsion produces hyperbolic trajectories with an eccentricity given by

$$(\varepsilon^2-1)=l^2/\eta^2 \tag{33}$$

where l is the angular momentum and η is the Sommerfeld parameter. This leads to a modified version of Eq. (6) given by

$$T_{GC}(b)=[K\sigma_{NN}/C(b)]\exp[-R(b)/2\sigma^2] \tag{34}$$

where

$$C(b)=b/(\eta_k^2+b^2)^{1/2}$$

and

$$R(b)=\eta_k+(\eta_k^2+b^2)^{1/2}$$

with

$$\eta_k=\eta/k=0.5Z_PZ_Te^2/E_{\text{c.m.}}\ .$$

[Notice that as η_k goes to zero, $C(b)$ tends to 1.0 and $R(b)$ tends to b.] The effect of this correction is to reduce the value of the Gaussian parameter σ obtained using Eq. (7) by more than 10% near 12 fm where the values of σ are near a minimum; however, at 8 fm (where significant contributions to the cross sections arise—see below) the reductions are more than 40%.

IV. THE RANDOM-WALK CALCULATIONS

The values obtained from the KAROL code for the quantities σ and K were (2.2021, 127.33), (2.1973, 122.16), and (2.213, 138.55) for the undeformed densities, and for the deformed densities corresponding to the transverse and helicity tensor polarized beam, respectively. Thus $\Delta\sigma=0.011$ and $\Delta K=11.2$. The value of k [Eq. (11)] was set to 1.0×10^{-8}, thus invoking the pure Gaussian approximation, since it was found that larger values produced a poorer description of the analyzing power data.

The total cross sections are predicted from Eq. (23) using the value of $2\pi\sigma^2=304$ mb; in Fig. 4 the results are plotted as the solid curve [multiplied by the factor of 2.0 from Eq. (27)] against the experimental points. The trend of the data is quite well predicted, but the experimental values for the lighter ions fall far below the curve, as do the values for the Al ions. Since the summation of the differential cross sections does not include the most forward angles, our measurements are expected to underestimate the total cross sections. In addition, the experimental spectra for $Z\leq5$ were truncated by the thickness of the ΔE detector, so we expect the measured cross sections to be too low, especially for Be ions where the ^{8}Be flux is lost into the He ions. The measured cross section for He ions of $\sim$186 mb lies far above the random-walk prediction. If our predictions are valid, approximately 28 mb results from the fragmentation into He ions and if we assume 20 mb obtained from the missing ^{8}Be ions, giving 40 mb of He, this leaves 118 mb from other process which lead to the production of He ions such as breakup of ^{23}Na (into, e.g., He + F) and evaporative processes. As we have pointed out, some of the double ^{4}He ions from ^{8}Be breakup are included in the ^{7}Li ions because the detector signals are identical. The summed experimental cross sections for all ions between Li and Al is 451 mb; adding the He cross section of 186 mb and a value of 1472 mb for the predicted fusion cross section [34], we obtain a value of 2109 mb, in excellent agreement with the value obtained from the optical model predictions of 2108 mb using the data of Choi [35]; however, there may be some double counting of alpha particles from fusion. In this work we have made the simplifying assumption that each unit change in charge ΔZ corresponds to a mass loss or gain M or 2. In principle, our predictions should be averaged over the individual mass distributions for each ejectile Z, but these distributions were not measured in our data. In any case, the result of such averaging is to simply smooth out the trends which we predict in this work.

Once the values of σ and K are determined from the densities of the projectile and target, the only free parameters which can enter the calculations are the value of σ_0, the Goldhaber width, and the values of the probabilities P_{+1}, P_{-1}, P_0, and P_{-4}; for the T_{20} calculations the values of b_0 and a_{PT} must also be set. A scrutiny of Eq. (17) shows that there is no dependence of the observables upon the value of P_0, and that only the loss/gain ratio of P_{-1}/P_{+1} and the alpha emission probability P_{-4} are effective. In addition there is a constraint that $P_{-1}+P_{+1}+P_0=1.0$ [16] for the primary reaction (which may be modified by emission of alpha particles and secondary evaporation).

One would expect the probability of nucleon gain P_{+1} to be less than the loss probability P_{-1}, simply because the loss probability refers to nucleons which escape from the projectile and are captured by the target *or* emerge as free nucleons, whereas the gain probability refers only to nucleons escaping from the target and captured by the projectile. With a value of $P_{+1}=0.1$ the loss/gain ratio was varied from 1 to 4, while values of P_{-4} in the range 0.05 to 0.2 were tried. It soon became clear that the cal-

culations for the differential cross sections of fragments near the projectile mass produced angular distributions that were too sharply peaked near the rainbow angle of 39° (laboratory), so that the Goldhaber width was increased from 100 to 150 MeV/c. This has the effect of broadening the width of those angular distributions near the projectile charge, but has little effect for large mass losses since the widths in Eq. (19) approach 20° or more. An enlarged value for the Goldhaber width probably indicates that the Fermi momentum within the projectile and target play a more important role at these lower energies, and that a better description of the data must take such effects into account.

The value of P_{-4} plays a critical role in the enhancement of the analyzing powers when M is a multiple of 4; i.e., for the alpha-particle loss nuclei via Eq. (16). Values of $P_{-4} \sim 0.2$ produce very large differences in analyzing powers between O and N ejectiles, but unfortunately also lead to an increase in the differential cross sections at larger angles which are not observed in the data. This accounts in part for the overprediction of the differential cross section for F ions between 20° and 50° shown in Fig. 5. In order to make simultaneous fits to differential cross sections and analyzing powers, a grid was made over the value of P_{-4} while varying the ratio of P_{-1}/P_{+1}; the values of $P_{+1}, P_{-1}, P_0, P_{-4}$ of 0.1,0.25,0.65,0.075 were considered the best compromise.

As pointed out above, there is no sensitivity of the calculations to the values of P_0, but the analyzing powers become larger with increasing values of P_{-1}. As M increases, so the analyzing powers decrease, but this is slightly offset for multiples of $M=4$, where the analyzing powers grow with increasing values of P_{-4}. The overall shapes of the distributions do not change very much for large M, owing to the smearing from the recoil effect [Eq. (19)], but for small M an increase in the Goldhaber width, σ_0, smears out and reduces the depths of the minima. Thus, the centroids of the minima in the analyzing powers are little affected by any changes of parameters, but the depths of the minima are determined by a balance between P_{-1}, P_{-4}, and σ_0. Increasing values of both P_{-1} and P_{-4} increases the gradient of the differential cross sections for large mass losses (e.g., for Li ions), so our final values for the probability matrix attempted to describe both this gradient, yet also describe the analyzing powers over a wide range of M. Increasing P_{-4} also increases the peak cross section near 40° for ejectiles where M is a multiple of 4. Our analyzing power data would favor larger values of P_{-4}, to enhance the differences when M is a multiple of 4, but the differential cross sections do not indicate a corresponding enhancement for these mass losses. Our data indicate deviations from the simple assumptions of the random-walk model. Figures 10 and 11 show the evolution of the predicted differential cross sections and transverse analyzing powers, ${}^{T}T_{20}$, for mass losses M of 2, 4, 6, 8, and 16.

Figure 12 shows the contributions to the cross sections as a function of impact parameter for a variety of mass loss or gain, M. Notice that when M is a multiple of 4, there is contribution to the cross sections from larger impact parameters which is not present when M is not a multiple of 4; this results from the effect of P_{-4} on P_M $[T(b)]$. With increasing mass loss, the random-walk model produces its cross sections from smaller impact parameters. This feature of the model reproduces traditional ideas about the removal of nucleons from the projectile corresponding to the simple overlap of the density distributions—the larger the overlap the more nucleons are removed.

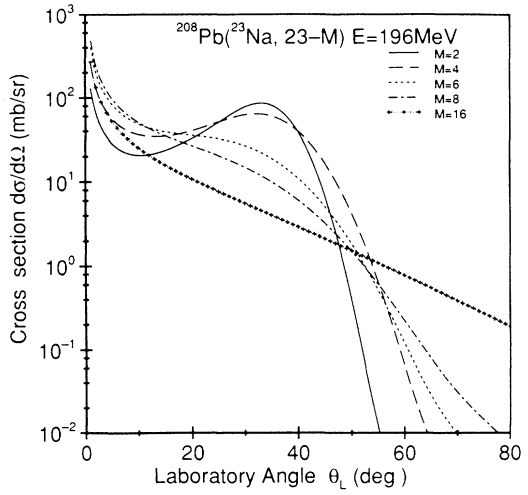

FIG. 10. Evolution of the differential cross sections versus laboratory angle for increasing mass loss.

We can now understand how the analyzing powers are produced in this model. The raw differential cross section [Eq. (15)] is a distribution which is sharply peaked near the rainbow angle, but is smeared out by the recoil widths [Eq. (19)], and distorted in shape by the different probabilities P_M $[T(b)]$ in Eq. (17). The difference in the projectile densities for the aligned and nonaligned beams produces a difference (analyzing power) in the raw differential cross section which is also peaked at the rain-

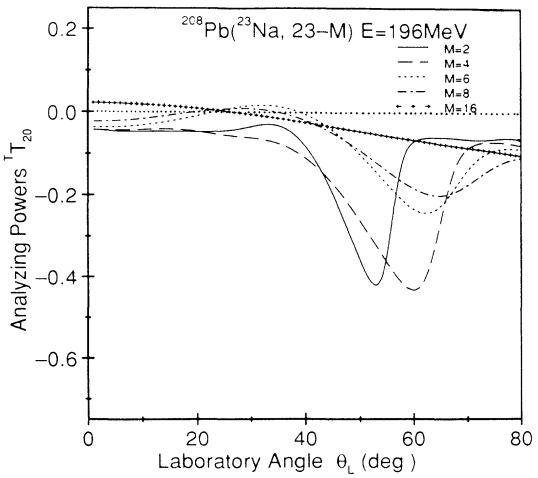

FIG. 11. Evolution of the analyzing powers in the transverse frame, ${}^{T}T_{20}$, vs laboratory angle for increasing mass loss.

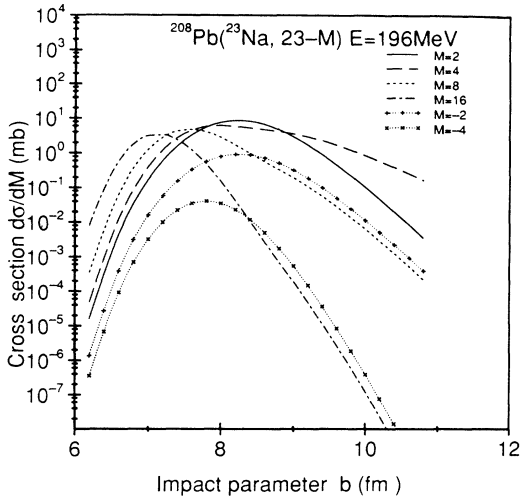

FIG. 12. Contributions to the cross sections for different mass losses M vs the impact parameter b.

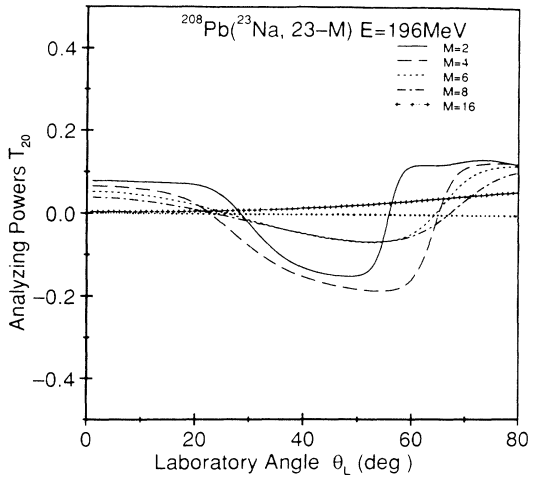

FIG. 13. Evolution of the analyzing powers in the helicity frame, T_{20}, vs laboratory angle for increasing mass loss.

bow angle, near 39°. For small mass (charge) losses the values of P_M [$T(b)$] have little effect, and only the widths [Eq. (19)] smear out the distributions, so the model predicts quite large analyzing powers near the rainbow angle. With increasing mass loss, the values of P_M [$T(b)$] in Eq. (17) push the dominant contributions to smaller impact parameters, where there is larger overlap and hence less sensitivity to the deformed shape of the projectile; with the smearing of the distributions this reduces the average values of the analyzing powers.

The predictions shown in Fig. 7 for the tensor analyzing powers in the helicity frame use values of $b_0 = 8.5$ fm and $a_{PT} = 0.1$ fm. The value of b_0 lies close to the peak of the curves in Fig. 12; a small value for a_{PT} of about 0.1 was required to give sufficiently large analyzing powers for larger values of the mass loss, M. Figure 13 shows the evolution of the T_{20} distributions for $M = 2$, 4, 6, 8, and 16. No combination of parameters was able to reproduce the negative to positive transition to the T_{20} analyzing powers near 50° laboratory; the transition is predicted near 55° for $M = 1$, and increases slightly with increasing M. The transition parameter b_0 from Eq. (28) has a value of 8.5 fm, slightly smaller than the sum of the projectile and target radii, as expected from Eq. (29). The small value of a_{PT} suggests that there is a rapid transition between the two situations depicted in Fig. 1(b), which can be accounted for by assuming some friction in the collision below a certain impact parameter which rotates the spin symmetry axis to make the major axis of the projectile the effective part of the density distribution. This friction damps the radial motion of the nuclei, but allows the transfer of angular momentum and is observed in deep inelastic scattering [29].

The comparisons of our predictions to the experimental data shown in Figs. 5, 6, and 7 enable us to make some general observations. For large values of the mass loss, M, the slope of the differential cross sections is well fitted, but the predicted values for Be and B are a factor of 2 larger than the data, consistent with our observations that there is missing flux from the spectra of these ions. The overall width of the bell-shaped distributions near $Z = 11$ is underpredicted, despite our increase of σ_0 to 150 MeV/c. The predicted $^{T}T_{20}$ analyzing powers show a smooth variation from a large negative oscillation for Ne and F to a negative-going trend for Li, which is mirrored in the data. The data for Ne ions, however, show no sign of this oscillation, and the enhancement predicted for the alpha-loss nuclei is much weaker than that observed in our data for N ions. The same general features are observed in the fits to the T_{20} data; the Ne data show little structure, while the prediction is for a large negative-going oscillation, changing to positive values at larger angles. This behavior is observed in the T_{20} data for the lighter ions, but the negative to positive transition is not predicted at a small enough angle, and the enhanced values for N ions are too small. There is a smooth variation predicted towards a positive-going trend for Li ions which is seen in the data.

V. CONCLUSIONS

Unique measurements have been made of the differential cross sections and tensor analyzing powers for the ejectiles produced by fragmentation of polarized ^{23}Na ions on a ^{208}Pb target at 195.5 MeV (8.5 MeV/u). The nuclear random-walk model has been used to predict the observables, extending the present model to include the deformed shape of the projectile and to incorporate corrections for the Coulomb trajectories.

The trend of the total cross section as a function of the charge number Z is well described by the random-walk model, assuming that the mass loss M is twice the charge loss ΔZ, but the model overpredicts the measured values. The angular distributions for the differential cross sections show a smooth variation from a bell shape for small charge losses to an exponential slope for large ΔZ; this general behavior is well reproduced by the random-walk model, although the detailed fits to the data are not good.

The measurements of transverse tensor analyzing powers ${}^{T}T_{20}$ show negative values except for Ne ions. Using a nuclear density with the known quadrupole deformation of ^{23}Na, the random-walk model predicts such negative values, but the trend with increasing mass loss is not fully reproduced, and the ${}^{T}T_{20}$ values for Ne are overpredicted, while those for N ions are underpredicted. The measured T_{20} analyzing powers show little structure for Ne ions, but indicate a strong negative to positive transition near 50° laboratory with increasing mass loss; this transition angle is not reproduced by the random-walk model.

Enhanced values of both ${}^{T}T_{20}$ and T_{20} are observed in the data for the ions with $\Delta Z=2,4$ which may correspond to the loss of one or two alpha particles. These variations and trends are reproduced by the random-walk model which predicts a weak (but insufficient) enhancement in the analyzing powers for the ions with mass loss $M=4,8$ ($\Delta Z=2,4$).

The random-walk model produces tensor analyzing powers which are intuitively what we expect from the overlap of a deformed projectile with a target, with the smallest mass loss being most sensitive to the deformation, and hence producing the largest analyzing powers. However, the weak analyzing powers observed for Ne ions may be an indication that there are interfering processes, such as few-nucleon transfer reactions, strongly coupled to the elastic scattering, which are not incorporated into the random-walk model. Measurements of the analyzing powers as a function of excitation energy may be able to resolve the low-lying transfer processes from the more highly excited breakup spectrum. The analyzing power data provide an extra insight into the fragmentation process; the simple shape model is not sufficient to explain these data in detail. This suggests that the dependence of the fragmentation mechanism on impact parameter may differ from that proposed by the random-walk model, or that the primary emission of alpha particles may be an important process, thus reinforcing our ideas about the cluster nature of light nuclei when they are highly excited.

These conclusions suggest that exclusive measurements of ejectile ions in coincidence with alpha particles would be a useful study. Further measurements at higher energies would also be valuable, but polarized studies are necessarily limited, since polarized heavy ion beams are only available using Tandem Van de Graaf accelerators. The differential cross section and tensor analyzing power data presented here should provide a useful test for the many models of the fragmentation process which are under development.

The authors acknowledge the financial support of SERC Grants GR/F39874 and GR/H/23825.

[1] K. H. Kampert, J. Phys. G **15**, 691 (1989).
[2] J. W. Wilson, L. W. Townsend, and F. F. Badavi, Nucl. Instrum. Methods **B18**, 225 (1987); Ch. Egelhaaf, G. Bohlen, H. Fuchs, A. Gamp, H. Homeyer, and H. Kluge, Phys. Rev. Lett. **46**, 813 (1981); V. Borrel, D. Guerreau, J. Galin, B. Gatty, D. Jaquet, and X. Tarrago, Z. Phys. A **314**, 191 (1983); F. Rami, J. P. Coffin, G. Guillaume, B. Heusch, P. Wagner, A. Fahli, and P. Fintz, Nucl. Phys. **A444**, 325 (1985).
[3] G. F. Bertsch and S. Das Gupta, Phys. Rep. **160**, 189 (1988), and references therein.
[4] A. Oubahadou, R. Dayras, and G. Royer, J. Phys. G **17**, 1415 (1991).
[5] A. S. Goldhaber, Phys. Lett. **53B**, 306 (1974).
[6] S. E. Koonin and J. Randrup, Nucl. Phys. **A356**, 223 (1981).
[7] B. H. Sa and D. H. E. Gross, Nucl. Phys. **A437**, 643 (1985).
[8] W. A. Friedman and W. G. Lynch, Phys. Rev. C **28**, 16 (1983); **28**, 950 (1983).
[9] H. W. Barz, J. P. Bondorf, R. Donangelo, R. Elmer, F. S. Hansen, B. Jakobsson, L. Karlsson, H. Nifenecker, H. Schulz, F. Schussler, K. Sneppen, and K. Sodestrom, Nucl. Phys. **A531**, 453 (1991).
[10] S. Leray, C. Ngo, P. Bouissou, B. Remaud, and F. Sebille, Nucl. Phys. **A531**, 177 (1991).
[11] C. Gregoire, B. Remaud, F. Sebille, L. Vinet, and Y. Raffray, Nucl. Phys. **A465**, 317 (1987).
[12] Li Zhuxia, C. Hartnack, H. Stocker, and W. Greiner, Phys. Rev. C **44**, 824 (1991).
[13] A. J. Cole, Z. Phys. A **322**, 315 (1985).
[14] P. J. Karol, Phys. Rev. C **11**, 1203 (1975).
[15] B. G. Harvey, Nucl. Phys. **A444**, 498 (1985).
[16] A. J. Cole, Phys. Rev. C **35**, 117 (1987).
[17] A. J. Cole, R. Cherkaoui-Tadili, and J. Alarja, Phys. Rev. C **40**, 1265 (1989).
[18] S. E. Darden, in *Polarization Phenomena in Nuclear Reactions,* edited by H. H. Barschall and W. Haeberli (University of Wisconsin Press, Madison, 1971).
[19] B. Jeckelmann, W. Beer, I. Beltrami, F. W. N. de Boer, G. de Chambrier, P. F. A. Goudsmit, J. Kern, H. J. Leisi, W. Ruckstuhl, and A. Vacchi, Nucl. Phys. **A408**, 495 (1983).
[20] H. D. Choi, C. O. Blyth, S. J. Hall, O. Karban, G. Kuburas, S. Roman, G. Tungate, N. J. Davis, A. C. Shotter, K. A. Connell, and S. E. Darden, Nucl. Phys. **A529**, 190 (1991).
[21] G. Tungate and D. Fick, in *Microscopic Optical Potentials, Proceedings, Hamburg, 1978* edited by H. V. Geramb, Lecture Notes in Physics Vol. 89 (Springer, Berlin, 1979), p. 404.
[22] K. H. Mobius, R. Bottger, P. Egelhof, Z. Moroz, E. Steffans, G. Tungate, I. Koenig, and D. Fick, Phys. Rev. Lett. **46**, 1064 (1981).
[23] S. J. Hall, G. Tungate, C. O. Blyth, H. D. Choi, K. A. Connell, N. J. Davis, B. R. Fulton, O. Karban, G. Kuburas, J. M. Nelson, S. Roman, and P. J. Woods, J. Phys. G **18**, 181 (1992).
[24] K. Blatt, K. Beck, B. Beck, H. Jansch, H. Leucker, D. Fick, R. Caplar, R. Butsch, K. H. Mobius, W. Ott, P. Paul, E. Steffans, J. Pochodzall, and G. Tungate, Z. Phys. A **329**, 103 (1988).
[25] O. Karban, W. C. Hardy, K. A. Connell, S. E. Darden, C. O. Blyth, H. D. Choi, S. J. Hall, S. Roman, and G. Tungate, Nucl. Instrum. Methods **A274**, 4 (1989).

[26] O. Karban, C. O. Blyth, H. D. Choi, J. B. A. England, S. J. Hall, S. Roman, G. Tungate, N. J. Davis, A. C. Shotter, and K. Connell, Appendix to the Daresbury Annual Report 1988/89 (unpublished); O. Karban, C. O. Blyth, H. D. Choi, K. A. Connell, S. E. Darden, N. J. Davis, J. B. A. England, S. J. Hall, S. Roman, and G. Tungate, J. Phys. G **14**, L261 (1988).
[27] A. C. Shotter, in *Clustering Aspects of Nuclear Structure,* edited by J. S. Lilley and M. A. Nagarajan (D. Reidel, Dordrecht, 1984).
[28] D. M. Brink, Phys. Lett. **40B**, 37 (1972).
[29] P. J. Siemens and A. S. Jensen, in *Elements of Nuclei* (Addison-Wesley, Reading, MA, 1987), Chap. 11.
[30] B. G. Harvey and M. J. Murphy, Phys. Lett. **130B**, 373 (1983).
[31] H. Nishioka and R. C. Johnson, Nucl. Phys. **A440**, 557 (1985); **A465**, 173 (1987); J. Gomez-Camacho and R. C. Johnson, J. Phys. G **12**, L235 (1986); **14**, 609 (1988).
[32] J. Cook, Comput. Phys. Commun. **25**, 125 (1982).
[33] K. H. Mobius, Z. Phys. A **310**, 159 (1983).
[34] W. W. Wilcke, J. K. Brikelund, H. J. Wollershein, A. D. Hoover, J. K. Huizenga, W. U. Schroder, and L. E. Tubbs, Nucl. Data Nucl. Tables **25**, 389 (1980).
[35] H. D. Choi, Ph.D. thesis, University of Birmingham, 1990.